CHARITÉ
UNIVERSITÄTSMEDIZIN BERLIN

Scattering compensation by focus scanning holographic aberration probing (F-SHARP)

Ioannis N. Papadopoulos, Jean-Sébastien Jouhanneau, James F. A. Poulet, Benjamin Judkewitz

Document type
Postprint (accepted version)

This version is available at
https://doi.org/10.17169/refubium-29928

Citation details
Papadopoulos IN, Jouhanneau J-S, Poulet JFA, Judkewitz B. Scattering compensation by focus scanning holographic aberration probing (F-SHARP). Nature Photonics. [Online] Springer Nature; 2016;11(2): 116–123. DOI: 10.1038/nphoton.2016.252

Terms of use
All rights reserved. This document is intended solely for personal, non-commercial use.

Scattering compensation by focus scanning holographic aberration probing (F-SHARP)

Ioannis N. Papadopoulos[1], Jean-Sébastien Jouhanneau[2], James F. A. Poulet[2] and Benjamin Judkewitz[1]*

1: Bioimaging and Neurophotonics Lab, NeuroCure Cluster of Excellence, Charité Berlin, Humboldt University, Charitéplatz 1, 10117 Berlin, Germany

2: Max Delbrück Center for Molecular Medicine, Robert-Rössle-Str. 10, 13092 Berlin, Germany

*corresponding author (benjamin.judkewitz@charite.de)

Abstract

A longstanding goal in biomedical imaging, the control of light inside turbid media requires knowledge of how the phase and amplitude of an illuminating wavefront are transformed as the electric field propagates inside a scattering sample onto a target plane. So far, it has proved challenging to non-invasively characterise the scattered optical wavefront inside a disordered medium. Here, we present a non-invasive scattering compensation method, termed F-SHARP, which allows us to measure the scattered electric-field point spread function (E-field PSF) in three dimensions. Knowledge of the phase and amplitude of the E-field PSF makes it possible to optically cancel sample turbulence. We demonstrate the imaging capabilities of this technique on a variety of samples, and notably though vertebrate brains and across thinned skull *in vivo*.

Optical microscopy is an indispensable tool for biomedical research. Yet, the same structures that make biological samples interesting to study under a microscope (such as cells, vasculature and subcellular organelles) scatter light and thus render tissues opaque. Tissue opacity poses a major challenge to all optical imaging and photo-stimulation methods, fundamentally limiting them to thin sections, cultured cells or superficial layers of tissue.

Advanced fluorescence microscopy techniques, such as confocal and two-photon (2P) microscopy[1], allow researchers to push the limits of imaging deep inside turbid biological tissue[2] by selectively exploiting those photons that have not been scattered (ballistic photons). However, beyond the depth of a few scattering mean free paths (typically several hundred μm in biological tissues) this strategy becomes futile because hardly any ballistic photons remain[3].

Tissue turbidity has been studied in two regimes: aberration and scattering. Aberrations are caused by refractive index variations at a spatial scale larger than the wavelength – such as tissue surface curvature or bulk tissue variations. Their effect can be mitigated by adaptive optics (AO) microscopy[4-9]. Modal AO techniques employ a deformable mirror that iterates through low order deformations[10,11] and pupil segmentation approaches[6,7] acquire images through segments of the objective back aperture to estimate the phase gradient in order to correct aberrations.

Yet, as tissue depth increases, scattering due to wavelength-scale and sub-wavelength inhomogeneities starts to overtake aberration as the major source of turbidity. It was long considered fundamentally impossible to correct for such diffuse scattering, but recent work on complex wavefront shaping confirmed that even entirely scattered light can be controlled and utilized for imaging. Optical phase conjugation[12-14], iterative optimization wavefront shaping[15] and transmission matrix based approaches[16,17] were used to image through scattering media[18,19], convert them into lenses[20], mirrors[21], waveplates[22] and pulse shapers[23,24]. However, all these techniques rely on physical access through the scattering medium, which makes them impractical for realistic imaging applications. To overcome this limitation, researchers have exploited so-called 'guide-stars'[25] inside the scattering medium. Acousto-optic[26-29], photoacoustic[30,31] and nonlinear[32-34] reference beacons can be used to find the wavefront correction – for example by using them as feedback in an iterative optimization approach. The correct wavefront that will lead to a focus inside the medium is found by optimizing the phase of each pixel of the wavefront shaper, either sequentially or in a multiplexed manner. Because such techniques have to iterate through each correction mode (e.g. each pixel on a wavefront shaper) they have to trade off measurement time with wavefront resolution. This is why high-resolution scattering compensation (>1000 pixels) has only been demonstrated in static samples, such as dead tissue. Live tissue scattering compensation methods[35,36] have so far

59 been limited to low pixel numbers (<1000) and are thus unable to resolve steep wavefront
60 gradients, such as those caused by strong aberrations[7].

61 There is an unmet need for a method that bypasses this trade-off and combines the
62 strengths of AO (speed, steep gradients) with the strengths of scattering compensation
63 (number of modes, not dependent on quasi-ballistic light). Here we present a new turbidity
64 suppression approach, termed Focus Scanning Holographic Aberration Probing (F-SHARP),
65 which achieves this combination thanks to an inverse strategy. Unlike previous work that was
66 based on iterating through the modes of a wavefront shaper, F-SHARP directly measures the
67 phase and amplitude of the scattered electric field point-spread-function (E-field PSF or E_{PSF}).
68 We demonstrate that knowledge of this E-field permits rapid, high-resolution optical
69 correction of both aberrations and scattering in living tissue.

70 Principle of operation

71 In a laser-scanning microscope, incident light is brought to a focus at a location of interest.
72 The spatial variation of the light intensity in the focal plane is defined as the intensity PSF
73 (I_{PSF}). In analogy, we call the complex-valued electric field at the focal plane the electric-field
74 point spread function (E-field PSF or E_{PSF}, with $I_{PSF} = |E_{PSF}|^2$). In linear fluorescence
75 microscopy, fluorescence excitation is proportional to the illumination intensity, and the
76 excitation PSF equals the intensity PSF. To form an image, one can either raster-scan the
77 excitation PSF or the excitation beam may be kept stationary while scanning the sample. In
78 both schemes, we can describe the acquired image as the convolution of the excitation PSF
79 with the object. In a perfect optical imaging system, the excitation PSF is diffraction-limited
80 and has almost all of its energy concentrated in one location, resembling a point-like δ-
81 function. However, as the focal plane is advanced deeper into an inhomogeneous medium,
82 photons start to get deflected due to aberrations and scattering. Instead of coherently
83 combining at the desired focus location, they spread, adding noisy side-lobes to the E-field
84 PSF. This leads to a deterioration of the image quality, both in terms of resolution and signal-
85 to-noise ratio (SNR). A 2P microscope is an implementation of a laser-scanning microscope
86 that takes advantage of 2P absorption[37]. Due to this nonlinearity, the excitation PSF of the 2P
87 microscope is equal to the square of the intensity PSF, i.e., the 4th power of the amplitude of
88 the electric field ($I_{PSF}^2 = |E_{PSF}|^4$). This nonlinear process suppresses some of the scattered
89 sidelobes and leads to an improved excitation PSF compared to linear (‘one photon’ or 1P)
90 excitation. Yet, as the imaging depth increases further towards the transport mean-free path,
91 scattered photons begin to dominate even in 2P microscopy. The focus intensity drops, the
92 resolution decreases and squaring alone is not enough to recover a point-like focus. For
93 brevity we use the term “scattered E-field PSF” as an inclusive term for both aberrations and

94 scattering and in general as a description for any E-field PSF that deviates from the perfect
95 diffraction-limited one.

96 The goal of F-SHARP is to measure and optically correct the scattered E-field PSF of a
97 2P microscope and thus optically cancel the effect of turbidity. An F-SHARP microscope is
98 based on the basic layout of a regular 2P microscope, with several important modifications: in
99 addition to the scanning beam, we introduce a second beam, which is not scanned, but parked
100 within the field-of-view (Figure 1a). Because both beams travel through the same scattering
101 medium, they undergo similar scattering and their E-field PSF profiles can be assumed to be
102 identical (this is a helpful but non-essential simplification which we will relax later). As we
103 show below, increasing the intensity of one of the two beams relative to the other, causes the
104 strong beam to become point-like (due to the nonlinear response) and by scanning one beam
105 against the other we end up, in effect, scanning a point-like probe across the weak beam's E-
106 field PSF. Analogously to image formation in 2P microscopy, where the nonlinear excitation
107 PSF probes the object, F-SHARP probes the weaker scattered beam with the strong beam
108 (Figure 1b).

109 Assuming a uniform fluorescent sample, in the case of 2P excitation, the signal generated
110 by the superposition of the scanning and the stationary beams across a scanning coordinate x
111 and at a given location x', respectively, reads

112 $$I(x) \propto \int \left| E_{\text{scan}}(x'-x) + E_{\text{stat}}(x') \right|^4 dx' \qquad (0)$$

113 where both the stationary (stat) and the scanning (scan) beams are scaled versions of the E-
114 field PSF, $\mathrm{E}_{\text{stat}}(x') \propto \mathrm{E}_{\text{scan}}(x') \propto \mathrm{E}_{\text{PSF}}(x')$. If the stationary E-field has a weaker intensity than
115 the scanning E-field (e.g. $|E_{\text{stat}}|^2 / |E_{\text{scan}}|^2 < 0.1$), we can discard all the powers of E_{stat} equal
116 and larger than 2 in the algebraic expansion of Equation 1 (since they contribute only a very
117 small component to the final signal, e.g. < 1%) therefore yielding

118 $$\begin{aligned} I(x) \propto & \underbrace{\int \left| E_{\text{scan}}(x'-x) \right|^4 dx'}_{\text{uniform}} + 2\int \underbrace{\left| E_{\text{scan}}(x'-x) \right|^2 E^*_{\text{scan}}(x'-x)}_{\delta-\text{like function}} E_{\text{stat}}(x')\,dx' \\ & + 2\int \underbrace{\left| E_{\text{scan}}(x'-x) \right|^2 E_{\text{scan}}(x'-x)}_{\delta-\text{like function}} E^*_{\text{stat}}(x')\,dx' \end{aligned} \qquad (0)$$

119 Considering the E-field as a scattered focus with a stronger centre and weaker sidelobes,
120 the cubic term $\left| E_{\text{scan}}(x'-x) \right|^2 E^*_{\text{scan}}(x'-x) = \left| E_{\text{scan}}(x'-x) \right|^3 e^{-i\phi_{\text{scan}}(x'-x)}$ can be considered as a
121 highly peaked, δ-like function that is convolved with the stationary scattered E-field, E_{stat}.
122 Therefore, the final acquired signal will consist of a uniform background together with the
123 complex scattered E-field and its conjugate. This is equivalent to on-axis holography[38] where
124 the captured intensity is a combination of a DC term together with the field and its conjugate

125 $$I(x) \propto I_{\text{background}} + E_{\text{PSF}}(x) + E^{*}_{\text{PSF}}(x) \qquad (0)$$

126 where E_{stat} has been replaced by E_{PSF}.

127 The complex E-field parked within the field of view (FOV) can be easily isolated from
128 the DC and its conjugate by means of a phase stepping scheme[39] (see Supplementary
129 Information).

130 Knowing the scattered E-field PSF, we can use the time reversal symmetry of optical
131 propagation to correct for scattering by phase conjugation. With the wavefront-shaping
132 element lying on the Fourier conjugate plane to the image plane (Figure 1a, c), the required
133 correction pattern is the 2D Fourier transform of the measured E-field PSF. However, since
134 the scanning kernel in the previous analysis is not exactly a δ-function, the estimated E-field
135 PSF will approximate, but not perfectly match the true E-field PSF. After applying the
136 Fourier transform of the estimated E-field PSF on the wavefront shaper, the updated beam
137 will nevertheless be closer to a diffraction-limited spot, which in turn means that the third
138 power of its amplitude will more closely resemble a δ-function. Repeating the process using
139 the updated beam as the scanning δ-like-function the reconstruction of the scattered E-field
140 will be more accurate with each correction step of the method. Although, for simplicity, we
141 have described the scattered E-field to have a centre peak with smaller sidelobes, it can be
142 proven (see Supplementary Material) that irrespective of the shape of the original E-field
143 PSF, the amplitude of the corrected E-field PSF will be taken to the 3rd power after each
144 correction step. Consecutive cubing of the corrected E-field PSF amplitude will theoretically
145 turn any speckle pattern into a sharply peaked focus in a finite number of steps.

146 It is usually assumed in microscopy that the PSF of an imaging system is invariant to the
147 measurement strategy, be it scanning of the excitation focus over a sub-diffraction bead, or
148 inversely moving the bead across a stationary focus. However, the addition of a volume
149 inhomogeneous medium within the imaging path invalidates this assumption outside the so-
150 called memory-effect range[41-44]. To better understand how this affects the ability of F-SHARP
151 to obtain wavefront corrections, we consider the propagation from the image plane (Figure 1c,
152 plane A) to the focal plane in the scattering medium (plane B or sample plane) as a linear
153 transformation, represented by the transmission matrix T_{AB} (Figure 1c). Placing a point source
154 at location j along the image plane (A) and measuring the resulting scattered E-field in the
155 focal plane (B), which we label $E_B(j)$, leads to the measurement of the jth column of the
156 transmission matrix, $T_{AB}(:,j) = E_B(j)$.

157 Within this framework, we may now reinterpret the scanning procedure described above
158 (scanning of a strong beam against a stationary weak beam) as a strategy to measure $E_B(j)$,
159 and thus the the jth column of T_{AB}. The position of the shifted δ-function beam effectively

defines which entry of the column of $T_{AB}(:,j)$ we sample at each scan location along the focal plane (Figure 1d).

The transmission matrix model also offers a helpful description for an alternative scanning strategy, that is, keeping the strong δ-like beam fixed at one location in the scattering medium and scanning the weaker scattered beam against it. Since the strong δ-like beam is fixed at one location along the focal plane, it is helpful to interpret its interaction with the scattered beam as a stationary single-pixel photodetector that "samples" the scattered field. As the two beams interfere, this alternative F-SHARP strategy effectively measures the complex field value at one fixed location j along plane (B) (i.e., the location of the δ-like beam "pixel"), as we shift the source of the scattered field along plane (A) (Figure 1c, d). This offers, in effect, a method to measure one *row* of the transmission matrix, $T_{AB}(j,:)$. Instead of examining one scattered field at multiple locations along the focal plane like our first F-SHARP strategy, this alternative F-SHARP strategy examines the response at one focal plane location for multiple inputs.

Under the assumption of an infinite memory effect range, the two measurements described above, corresponding to rows and columns of the transmission matrix, are identical and both approaches will give the same results. As soon as the memory effect becomes finite, the measurements performed with the two strategies will only coincide within the memory effect range and will start to deviate outside of it. Since we are interested in focusing light to as tight a spot as possible at one location j along the focal plane (at a given time point), we are interested in knowing the jth transmission matrix *row*. Therefore, we adopt the second F-SHARP scanning technique outlined above for our following experimental demonstrations (strong beam fixed, weak scattered beam scanned). We note that this strategy does not require any memory effect for converging onto a tight focus.

As described previously, the strong beam is corrected after each correction step based on the measurement of the previous one, therefore being transformed quickly into a sharp focus. After the E-field PSF has been properly estimated, the weak beam is turned off and the strong corrected beam is scanned to form a 2P image of the sample, using the same scanning and detection strategy as conventional 2P imaging.

Results

To test the performance of F-SHARP, we placed 1 μm diameter fluorescent beads under a 500 μm thick slab of chicken muscle tissue (Figure 2a). In the conventional 2P image (corrected for all system aberrations) the sample appears as a dim, diffuse fluorescence (Figure 2f). In contrast, F-SHARP allows us to distinguish between individual beads at the object plane while at the same time increasing the detected fluorescence signal 77.5-fold (Figure 2g and

h). Because photons that were scattered are redirected towards the focus, the use of F-SHARP microscopy has a dual effect on the excitation PSF: First, it increases the signal level. Second, it sharpens the excitation PSF to deliver sharper images. The reconstructed E-field PSF (Figure 2b) appears as a random speckle modulated by a bell-shaped envelope. Its Fourier transform provides the phase correction pattern for the wavefront-shaping element (Figure 2e). We can quantify the number of corrected modes by comparing the mean mode size in the Fourier domain against the size of the back aperture. The mean modal size is calculated from the full width at the half maximum (FWHM) of the complex autocorrelation of the field which yields a measurement of 1181 corrected modes (Supplementary Figure 3). Knowledge of the complex E-field PSF at the image plane allows us to create a 3D reconstruction of the scattered E-field (Figure 2c) using scalar wave propagation. Furthermore, it allows us to infer the 3D shape of the corrected focus after phase-only wavefront modulation (Figure 2d), which is a sharp spot. The inferred 3D shape will be valid within the extent of a scattering mean free path (typically >100 µm for brain tissue, ~50 µm for chicken muscle).

To characterize the performance of the F-SHARP microscope and to confirm that we indeed measure the E-field PSF, we placed an imaging system in transmission, which directly recorded the intensity PSF (schematic shown in Figure 3a). We then applied F-SHARP on an artificial test sample, which consisted of a diffuser film placed 0.58 mm above a uniform green fluorescent layer containing sparsely distributed red beads (Figure 3a). We chose the uniform fluorescence for correction because this is the most challenging (least forgiving) scenario to test our approach. Based on the E-field PSF measured by F-SHARP (Figure 3b), we can compare its intensity (Figure 3c) against the intensity of the scattered focus imaged in transmission (Figure 3d). Moreover, the 2P PSF of the system can be independently captured by scanning the scattered E-field PSF over a small bead (Figure 3g), and comparing it against the 4th power of the amplitude of the reconstructed PSF (Figure 3f). From the comparisons in Figure 3c-f and d-g we observe that the predicted PSFs based on F-SHARP match the intensity PSF measured with the imaging sensor in transmission and also the 2P PSF (4th power of field amplitude). Using the imaging system in transmission we can observe the evolution of the corrected PSF after each correction step (Figure 3h). Based on the aforementioned analysis we expect the intensity of the corrected PSF to be taken to the 3rd power each correction step, which can be confirmed by comparing Figure 3h with the 3rd power of the previous correction step as plotted in Figure 3i.

Next, we set out to demonstrate the ability of F-SHARP to correct for aberrations and scattering inside living tissue. We used F-SHARP to obtain images of the live brain of a 18 days post-fertilization (dpf) zebrafish larva expressing cytosolic GCaMP6f[45] (Figure 4a), a genetically encoded fluorescent calcium indicator[46]. We imaged a region 300 µm below the

231 surface. Conventional 2P microscopy (corrected for all system aberrations) allowed us to find
232 a blurred cluster of neurons (Figure 4b and e). In the F-SHARP corrected image, (Figure 4c
233 and f), the neurons can be individually separated and the signal intensity is increased 3.3-fold
234 (Supplementary Video 1). The reconstructed E-field PSF (Figure 4d) appears strongly
235 aberrated, explaining the poor image quality of the uncorrected image (Figure 4c and f). The
236 correction pattern applied onto the SLM (Figure 4g) contains mainly low order modes (low
237 spatial frequencies) implying aberrations as the dominant mechanism of image deterioration.
238 Based on the complex amplitude of the PSF at the imaging plane, we can infer the 3D shape
239 of the aberrated PSF (Figure 4h) and the corrected PSF (Figure 4i).

240 We then tested F-SHARP microscopy for *in vivo* mouse brain imaging. We used an
241 anesthetized GAD67 mouse with GFP-labelled interneurons[47] and imaged 480 μm below the
242 brain surface through a craniotomy (Figure 5a). Employing F-SHARP we can successfully
243 enhance the image quality, with the corrected image (Figure 5c) exhibiting a 5-fold increase
244 of the signal intensity compared to conventional 2P microscopy (corrected for all system
245 aberrations) (Figure 5b). The resolution of the image is increased, with the proximal dendrites
246 becoming more pronounced, as observed in the cross-section plot (Figure 5d, see also
247 Supplementary Video 2). The measured scattered E-field PSF (Figure 5f) contains a central
248 lobe, indicating the presence of ballistic light, with higher order modes surrounding it. The
249 F-SHARP correction pattern displayed on the SLM (Figure 5e) exhibits a combination of low
250 order and higher order modes, indicating a mixed contribution of both aberrations and
251 scattering. As before, we can predict the shape of the scattered and the corrected E-field PSF
252 in three dimensions (Figure 5g and h).

253 Having demonstrated the ability of F-SHARP to measure and correct aberrations, we
254 next tested its capabilities in a scenario where scattering is expected to be the dominant factor
255 of image deterioration. We imaged a single apical trunk dendrite of a layer 5 pyramidal
256 neuron through the thinned skull (~50 μm thickness) of an anaesthetized Thy1-YFP[48] mouse
257 (Figure 6a). We followed the same dendrite starting 25 μm under the surface of the brain
258 down to a depth of 325 μm. We used F-SHARP to correct aberrations and scattering every 50
259 μm and used the corrected PSF to capture a z-stack, ±25 μm above and below the correction
260 depth. We then rendered the dendrite in 3D (Figure 6b) and compared data obtained without
261 and with correction (Figure 6c and d). The image quality of the conventional 2P microscope
262 (corrected for all system aberrations) is poor even at the more superficial layers under the
263 skull (Figure 6c, top) with the dendrite being barely visible and appearing as a non-distinct
264 speckle pattern. Using F-SHARP we reconstructed the dendrite down to a depth of 325 μm
265 (Supplementary Video 3). Furthermore, we resolved single spines through a thinned skull
266 down to a depth of 200 μm (Figure 6d, middle). The reconstructed E-field PSF (Figure 6f)

267 quickly turns into a random speckle pattern, indicative of scattering processes. This is also
268 observable in the phase correction pattern applied on the SLM (Figure 6e) with the number of
269 modes increasing as we image deeper.

270 Discussion

271 We have presented a novel scattering compensation method, F-SHARP, which allows us to
272 non-invasively measure the scattered complex-valued E-field PSF. Knowledge of the phase
273 and amplitude of the E-field PSF allows us to compensate for both scattering and aberrations
274 and acquire high contrast images inside turbid tissue. We used F-SHARP to correct for
275 aberrations and scattering in zebrafish larvae and mice *in vivo*, and obtain high-resolution
276 images of fluorescently labelled structures, including submicron dendritic spines through the
277 thinned mouse skull *in vivo* down to a depth of 200 μm.

278 We derived analytically and validated experimentally that F-SHARP 'cubes' the
279 corrected E-field PSF amplitude with each correction step. This explains why F-SHARP does
280 not have to rely on the presence of any residual ballistic light, because any enveloped random
281 speckle pattern can be transformed into a sharp focus after a finite number of correction steps
282 (see also Supplementary Material). The number of correction steps needed will depend on
283 two factors: First, it depends on the shape of the original E-field. The more point-like the
284 initial scattered E-field is, the faster F-SHARP will converge towards a diffraction-limited
285 spot. Second, the convergence rate also depends on the sparsity of the sample. We proved that
286 for a uniform fluorescent sample, the corrected beam amplitude will be equal to the 3rd power
287 of the strong beam amplitude that was used for the inference of the scattered E-field PSF. If
288 the sample is sparse rather than uniform, the fluorescence of the strong beam will be spatially
289 modulated by the sample structure. The sparsest sample possible is a single small fluorescent
290 bead, which together with the strong beam would act as a sampling δ-function – leading to
291 convergence in a single step. Therefore, a uniform fluorescence layer (as the one used in
292 Figure 3) is the least forgiving scenario. We demonstrated that F-SHARP can efficiently
293 reconstruct the E-field PSF even in this case. In nearly all imaging scenarios of interest, the
294 sample sparsity will lie between the extremes of uniform fluorescence versus a single bead.
295 For the considered examples, when carrying out *in vivo* imaging of the zebrafish brain, of the
296 mouse brain through a craniotomy, and through the mouse skull, we needed 3 correction steps
297 for F-SHARP to converge.

298 F-SHARP exploits the nonlinear interaction between two beams to non-invasively
299 recover the scattered E-field PSF. In the current configuration, F-SHARP is implemented on a
300 2P fluorescence microscope. In principle, other nonlinear interactions could be used – such as
301 higher harmonic generation[49,50], coherent Raman scattering[51,52] or three-photon (3P)

302 microscopy[53]. As discussed above, in the case of 2P fluorescence, the amplitude of the E-field
303 PSF is taken to the third power with each F-SHARP correction step. In the Supplementary
304 Material we prove that, for the general case of an nth order nonlinearity, the E-field PSF
305 amplitude is taken to the $(2n-1)^{th}$ power. Thus, we predict that the use of higher order non-
306 linearities, such as 3P fluorescence, will further speed up the convergence rate of F-SHARP.
307 3P microscopy is currently pushing the depth limits of nonlinear imaging, but it still relies on
308 ballistic photons. We anticipate that its combination with F-SHARP will maximize the
309 attainable penetration depth.

310 In existing iterative wavefront shaping methods, the measurement speed is limited by the
311 time needed to iterate through all the modes of the wavefront shaper. In contrast, F-SHARP
312 determines the correction by raster-scanning the E-field PSF using fast galvanometric
313 scanners. F-SHARP therefore decouples the wavefront measurement speed from the limited
314 speed of wavefront shapers. Practically, wavefront measurement is no longer limited by
315 hardware, but only by the required pixel dwell time for a sufficient SNR of the E-field PSF
316 measurement. Higher SNR leads to a more accurate reconstruction of the E-field PSF and
317 therefore a higher enhancement in the corrected image. In the presented experiments, the
318 excitation power delivered to the sample did not exceed 25 mW. The integration time needed
319 for every line acquired was 18 ms, with every line consisting of 100 pixels (modes) and 4
320 phase shifts for the reconstruction of the complex E-field. This yields a measurement time per
321 mode equal to 0.72 ms/mode, which is two-fold faster than any other previously reported
322 method[35]. This was sufficient for in vivo imaging of an anaesthetized head-fixed mouse as we
323 demonstrated in Figure 5 and 6. Still, we have not yet reached the limit of the measurement
324 speed. A more power-efficient implementation of the optical system could allow us to
325 realistically deliver 100 mW to the sample. Moreover, a 2-phase stepping scheme can be
326 implemented, further reducing the number of needed phase-steps by a factor of two. These
327 adjustments could well bring the measurement time per mode to less than 0.1 ms/mode. After
328 the E-field PSF is measured and the wavefront corrected, imaging can be performed at the
329 speed of the scanning mirrors as in any conventional multi-photon microscope.

330 We note that the wavefront correction is valid as long as the relevant transmission
331 channels do not decorrelate. In our mouse in vivo experiments the correction lasted for at
332 least 20 minutes. This means that wavefront measurements only have to be performed rarely
333 compared to the amount of time that can be spent imaging inside tissues, but at lower
334 excitation power and higher sharpness than conventional 2P microscopy.

335 In summary, we demonstrated that F-SHARP is capable of measuring and correcting a
336 large number of scattered modes (>1000) with a measurement speed that is decoupled from
337 the speed of wavefront shapers. Unlike previous work, F-SHARP is not limited to correcting

338 either aberrations or scattering. It can efficiently measure and correct low spatial frequency
339 aberrations with steep phase changes, as well as high spatial frequency turbulence as caused
340 by scattering.

341 ## References

342 1. Denk, W., Strickler, J. & Webb, W. Two-photon laser scanning fluorescence
343 microscopy. *Science* **248,** 73–76 (1990).
344 2. Helmchen, F. & Denk, W. Deep tissue two-photon microscopy. *Nature Methods* **2,**
345 932–940 (2005).
346 3. Ntziachristos, V. Going deeper than microscopy: the optical imaging frontier in
347 biology. *Nature Methods* **7,** 603–614 (2010).
348 4. Booth, M.J. Adaptive optical microscopy: the ongoing quest for a perfect image.
349 *Light: Science & Applications* **3,** e165 (2014).
350 5. Tao, X. *et al.* Adaptive optics confocal microscopy using direct wavefront sensing.
351 *Opt. Lett.* **36,** 1062–1064 (2011).
352 6. Ji, N., Milkie, D.E. & Betzig, E. Adaptive optics via pupil segmentation for high-
353 resolution imaging in biological tissues. *Nature Methods* **7,** 141–147 (2009).
354 7. Wang, C. *et al.* Multiplexed aberration measurement for deep tissue imaging in vivo.
355 *Nature Methods* **11,** 1037–1040 (2014).
356 8. Olivier, N., Débarre, D. & Beaurepaire, E. Dynamic aberration correction for
357 multiharmonic microscopy. *Opt. Lett.* **34,** 3145–3147 (2009).
358 9. Wang, K. *et al.* Rapid adaptive optical recovery of optimal resolution over large
359 volumes. *Nature Methods* **11,** 625–628 (2014).
360 10. Booth, M.J., Neil, M.A.A., Juškaitis, R. & Wilson, T. Adaptive aberration correction
361 in a confocal microscope. *Proc. Natl. Acad. Sci* **99,** 5788–5792 (2002).
362 11. Débarre, D. *et al.* Image-based adaptive optics for two-photon microscopy. *Opt. Lett.*
363 **34,** 2495–2497 (2009).
364 12. Yaqoob, Z., Psaltis, D., Feld, M.S. & Yang, C. Optical phase conjugation for turbidity
365 suppression in biological samples. *Nature Photon.* **2,** 110–115 (2008).
366 13. Hsieh, C.L., Pu, Y., Grange, R. & Psaltis, D. Digital phase conjugation of second
367 harmonic radiation emitted by nanoparticles in turbid media. *Opt. Express* **18,** 12283–
368 12290 (2010).
369 14. Cui, M. & Yang, C. Implementation of a digital optical phase conjugation system and
370 its application to study the robustness of turbidity suppression by phase conjugation.
371 *Opt. Express* **18,** 3444–3455 (2010).
372 15. Vellekoop, I.M. & Mosk, A.P. Focusing coherent light through opaque strongly
373 scattering media. *Opt. Lett.* **32,** 2309–2311 (2007).
374 16. Popoff, S.M. *et al.* Measuring the transmission matrix in optics: an approach to the
375 study and control of light propagation in disordered media. *Phys. Rev. Lett.* **104,**
376 100601 (2010).
377 17. Choi, W., Mosk, A.P., Park, Q.H., Choi, W. & Choi, W. Transmission eigenchannels
378 in a disordered medium. *Phys. Rev. B* **83,** 134207 (2011).
379 18. Hsieh, C.L., Pu, Y., Grange, R., Laporte, G. & Psaltis, D. Imaging through turbid
380 layers by scanning the phase conjugated second harmonic radiation from a
381 nanoparticle. *Opt. Express* **18,** 20723–20731 (2010).
382 19. Vellekoop, I.M. & Aegerter, C.M. Scattered light fluorescence microscopy: imaging
383 through turbid layers. *Opt. Lett.* **35,** 1245–1247 (2010).
384 20. Vellekoop, I.M., Lagendijk, A. & Mosk, A.P. Exploiting disorder for perfect focusing.
385 *Nature Photon.* **4,** 320–322 (2010).
386 21. Katz, O., Small, E. & Silberberg, Y. Looking around corners and through thin turbid
387 layers in real time with scattered incoherent light. *Nature Photon.* **6,** 549–553 (2012).
388 22. Guan, Y., Katz, O., Small, E., Zhou, J. & Silberberg, Y. Polarization control of

389 multiply scattered light through random media by wavefront shaping. *Opt. Lett.* **37,**
390 4663–4665 (2012).
391 23. Katz, O., Small, E., Bromberg, Y. & Silberberg, Y. Focusing and compression of
392 ultrashort pulses through scattering media. *Nature Photon.* **5,** 372–377 (2011).
393 24. Aulbach, J., Gjonaj, B., Johnson, P.M., Mosk, A.P. & Lagendijk, A. Control of light
394 transmission through opaque scattering media in space and time. *Phys. Rev. Lett.* **106,**
395 103901 (2011).
396 25. Horstmeyer, R., Ruan, H. & Yang, C. Guidestar-assisted wavefront-shaping methods
397 for focusing light into biological tissue. *Nature Photon.* **9,** 563–571 (2015).
398 26. Xu, X., Liu, H. & Wang, L.V. Time-reversed ultrasonically encoded optical focusing
399 into scattering media. *Nature Photon.* **5,** 154–157 (2011).
400 27. Si, K., Fiolka, R. & Cui, M. Fluorescence imaging beyond the ballistic regime by
401 ultrasound-pulse-guided digital phase conjugation. *Nature Photon.* **6,** 657–661 (2012).
402 28. Wang, Y.M., Judkewitz, B., Dimarzio, C.A. & Yang, C. Deep-tissue focal
403 fluorescence imaging with digitally time-reversed ultrasound-encoded light. *Nature*
404 *Commun.* **3,** 928 (2012).
405 29. Judkewitz, B., Wang, Y.M., Horstmeyer, R., Mathy, A. & Yang, C. Speckle-scale
406 focusing in the diffusive regime with time reversal of variance-encoded light
407 (TROVE). *Nature Photon.* **7,** 300–305 (2013).
408 30. Chaigne, T. *et al.* Controlling light in scattering media non-invasively using the
409 photoacoustic transmission matrix. *Nature Photon.* **8,** 58–64 (2013).
410 31. Lai, P., Wang, L., Tay, J.W. & Wang, L.V. Photoacoustically guided wavefront
411 shaping for enhanced optical focusing in scattering media. *Nature Photon.* **9,** 126–132
412 (2015).
413 32. Aviles-Espinosa, R. *et al.* Measurement and correction of in vivo sample aberrations
414 employing a nonlinear guide-star in two-photon excited fluorescence microscopy.
415 *Biomed. Opt. Express* **2,** 3135–3149 (2011).
416 33. Tang, J., Germain, R.N. & Cui, M. Superpenetration optical microscopy by iterative
417 multiphoton adaptive compensation technique. *Proc. Natl. Acad. Sci* **109,** 8434–8439
418 (2012).
419 34. Katz, O., Small, E., Guan, Y. & Silberberg, Y. Noninvasive nonlinear focusing and
420 imaging through strongly scattering turbid layers. *Optica* **1,** 170–174 (2014).
421 35. Kong, L. & Cui, M. In vivo fluorescence microscopy via iterative multi-photon
422 adaptive compensation technique. *Opt. Express* **22,** 23786–23794 (2014).
423 36. Park, J.H., Sun, W. & Cui, M. High-resolution in vivo imaging of mouse brain through
424 the intact skull. *Proc. Natl. Acad. Sci. U.S.A.* **112,** 9236–9241 (2015).
425 37. Göppert-Mayer, M. Über Elementarakte mit zwei Quantensprüngen. *Annalen der*
426 *Physik* **401,** 273–294 (1931).
427 38. Gabor, D. A new microscopic principle. *Nature* **161,** 777 (1948).
428 39. Yamaguchi, I. & Zhang, T. Phase-shifting digital holography. *Opt. Lett.* **22,** 1268–
429 1270 (1997).
430 40. Kang, H., Jia, B. & Gu, M. Polarization characterization in the focal volume of high
431 numerical aperture objectives. *Opt. Express* **18,** 10813–10821 (2010).
432 41. Freund, I., Rosenbluh, M. & Feng, S. Memory effects in propagation of optical waves
433 through disordered media. *Phys. Rev. Lett.* **61,** 2328–2331 (1988).
434 42. Feng, S., Kane, C., Lee, P. & Stone, A. Correlations and Fluctuations of Coherent
435 Wave Transmission through Disordered Media. *Phys. Rev. Lett.* **61,** 834–837 (1988).
436 43. Judkewitz, B., Horstmeyer, R., Vellekoop, I.M., Papadopoulos, I.N. & Yang, C.
437 Translation correlations in anisotropically scattering media. *Nature Phys.* **11,** 684–689
438 (2015).
439 44. Schott, S., Bertolotti, J., Léger, J.F., Bourdieu, L. & Gigan, S. Characterization of the
440 angular memory effect of scattered light in biological tissues. *Opt. Express* **23,** 13505–
441 13516 (2015).
442 45. Rupprecht, P., Prendergast, A., Wyart, C. & Friedrich, R. W. Remote z-scanning with
443 a macroscopic voice coil motor for fast 3D multiphoton laser scanning microscopy.

444 *Biomed. Opt. Express* **7,** 1656–16 (2016).
445 46. Chen, T.W. *et al.* Ultrasensitive fluorescent proteins for imaging neuronal activity.
446 *Nature Photon.* **499,** 295–300 (2013).
447 47. Tamamaki, N. *et al.* Green fluorescent protein expression and colocalization with
448 calretinin, parvalbumin, and somatostatin in the GAD67-GFP knock-in mouse. *J.*
449 *Comp. Neurol.* **467,** 60–79 (2003).
450 48. Feng, G. *et al.* Imaging Neuronal Subsets in Transgenic Mice Expressing Multiple
451 Spectral Variants of GFP. *Neuron* **28,** 41–51 (2000).
452 49. Campagnola, P.J. & Loew, L.M. Second-harmonic imaging microscopy for
453 visualizing biomolecular arrays in cells, tissues and organisms. *Nature Biotechnol.* **21,**
454 1356–1360 (2003).
455 50. Débarre, D. *et al.* Imaging lipid bodies in cells and tissues using third-harmonic
456 generation microscopy. *Nature Methods* **3,** 47–53 (2006).
457 51. Freudiger, C.W. *et al.* Label-free biomedical imaging with high sensitivity by
458 stimulated Raman scattering microscopy. *Science* **322,** 1857–1861 (2008).
459 52. Zumbusch, A., Holtom, G.R. & Xie, X. S. Three-dimensional vibrational imaging by
460 coherent anti-Stokes Raman scattering. *Phys. Rev. Lett.* **82,** 4142 (1999).
461 53. Horton, N.G. *et al.* In vivo three-photon microscopy of subcortical structures within an
462 intact mouse brain. *Nature Photon.* **7,** 205–209 (2013).
463
464

Acknowledgements

We thank Roarke Horstmeyer for discussions and for valuable help with the manuscript. We thank Spencer Smith, Adam Packer, Chris Rowlands, Evgeny Bobrov and Maximilian Hoffmann for critically reviewing the manuscript. We would like to thank Lisanne Schulze for help with the zebrafish larvae mounting protocol and Nahid Hakiy for zebrafish husbandry. We are grateful to Claire Wyart and Andrew Prendergast for providing the NeuroD:GCaMP6f zebrafish line. This work was supported by the DFG (EXC 257 NeuroCure). INP is a recipient of the Early-PostDoc mobility fellowship of the Swiss National Science Foundation.

Material and correspondence

Correspondence and requests for materials should be addressed to B.J.

Author contributions

BJ and INP conceived and developed the idea. INP designed experiments with help from BJ. INP built the set-up, collected and analysed data. JSJ performed mouse procedures under supervision of JFAP. INP and BJ wrote the manuscript. BJ supervised the project.

Competing financial interests

INP and BJ applied for a patent on aspects of the presented work.

485 ## Figure captions

486 **Figure 1 | Principle of F-SHARP microscopy**. **a,** F-SHARP is implemented by adapting a
487 conventional 2P microscope, introducing a second copy of the excitation beam, controlling
488 the relative phase and intensities of both beams and correcting the strong beam with a
489 wavefront shaper (spatial light modulator, SLM). b, Theoretical description of the operating
490 principle of F-SHARP. In a laser scanning microscope the image can be described as the
491 convolution of the excitation PSF (in 2P microscopy: 4th power of the amplitude of the E-
492 field PSF) and the object – an approximation that holds within the memory effect range.
493 When imaging through an inhomogeneous medium the PSF is scattered. If the scattered E-
494 field PSF contains a peak, the microscope can still render a (distorted) image (top row). In
495 analogy, F-SHARP probes the scattered E-field PSF with the 3rd power of the scattered E-
496 field PSF. This provides an estimate of the scattered E-field PSF (middle row). After every
497 measurement and subsequent application of estimated correction pattern, the updated beam
498 amplitude is taken to the third power compared to the previous correction step (bottom row).
499 **c,** Transmission matrix representation of an imaging system from the image plane (A) to the
500 focal plane (B) through an inhomogeneous medium, T_{AB}. A point source at the image plane
501 (A) will get scattered to the focal plane (B) corresponding to a column of T_{AB}. Inversely, a
502 point source in the focal plane (B) will propagate through the scattering medium and will
503 result in a E-field at the image plane, which in turn will correspond to a row of the T_{AB}.

504

505 **Figure 2 | F-SHARP microscopy of fluorescent beads through muscle tissue. a**, Schematic
506 of the sample. Fluorescent beads are dispersed under the scattering tissue, separated by a
507 coverslip. **b**, The reconstructed E-field PSF appears as a random speckle pattern modulated by
508 a bell shape envelope. **c-d**, 3D propagation profile along y-z plane of scattered (c) and
509 corrected (d) real part of the E-field PSF. After the estimation of the E-field PSF, the applied
510 correction transforms it into a sharp focus in 3D (d). **e,** Correction pattern applied on
511 wavefront shaping device. The number of corrected modes (mean mode size over aperture) is
512 1181. **f-h,** Comparison of imaging before (f) and after correction (g) and cross-sectional plot
513 along dotted lines (h). After correction the maximum signal is enhanced 77.5-fold and
514 individual beads are distinguishable. In (b) the complex field is plotted with the amplitude
515 encoded in the brightness and the phase in the colormap. Images in (c) and (d) were saturated
516 to 0.7 of the respective maximum value to better visualize the sidelobes. Scale bars, 5 μm in
517 (b-d) and (f, g).

518

519 **Figure 3 | Characterization of E-field PSF estimation. a**, Schematic of the sample. Sparse
520 set of 1 μm red fluorescent beads dispersed in a fluorescein solution placed 0.58 mm below a
521 125 μm thick scattering film. F-SHARP corrections are calculated based on the uniform
522 fluorescein signal and the bead is used only for subsequent 2P PSF characterization while the
523 PSF is monitored in transmission. **b, e,** Reconstruction of the complex scattered field at the
524 image plane (b) and corresponding Fourier transform, $\mathcal{F}$ (E_{PSF}), yielding the correction
525 wavefront (e). **c-d, f-g,** Comparisons of squared amplitude of reconstructed E_{PSF} (c) against
526 measured intensity of PSF in transmission (d) and 4th power of amplitude of reconstructed E-
527 field PSF (f) against 2P image of a single 1 μm fluorescent bead (g). The comparisons
528 between (c-f) and (d-g) verify that F-SHARP indeed reconstructs the correct PSF at the
529 imaging plane. **h, i,** Evolution of the intensity of the corrected PSF measured in transmission
530 after each correction step (h). The original scattered PSF is transformed into a focus spot
531 within 3 correction steps. The correspondence between the PSF intensity and its 3rd power
532 during the previous correction step (i) confirms the theoretically expected convergence.
533 Images in (h and i) are presented saturated to increase the visibility of weaker sidelobes. Scale
534 bars, 10 μm in (b), 2 μm in (d-i).

535

536 **Figure 4 | In vivo F-SHARP imaging of a transgenic zebrafish larval brain**. **a,** Schematic
537 of *in vivo* imaging in an anaesthetized, immobilized zebrafish larva expressing GCaMP6f,
538 300 μm under the brain surface. **b, c, e, f,** Image comparison before (b, e) and after (c, f) F-
539 SHARP. Images in (b) and (c) are normalized to the maximum of the corrected image and the
540 brightness is increased by a factor of 2 in (e, f) for better visualization of the weak
541 fluorescence. In the conventional 2P image the cell population appears blurred. After F-
542 SHARP all the neurons can be individually separated and are 3.3 fold brighter. **d,** The
543 reconstructed E-field PSF is strongly aberrated explaining the poor image quality of the
544 original image. **g,** The correction phase pattern applied on the SLM contains mainly of low
545 order modes indicating aberrations as the main reason of image degradation. **h,** Cross-section
546 of the real part of the 3D propagation of the scattered E-field PSF along the y-z plane. **i,** After
547 phase corrections the E-field PSF turns into a sharp spot. Complex field in (d) is shown with
548 amplitude encoded in the brightness and the phase in the colormap. Scale bars, 10 μm in (b, c,
549 e, f) and 5 μm in (d, h, i).

550

551 **Figure 5 | Aberration and scattering compensation inside living mouse brain. a,**
552 Schematic of *in vivo* mouse brain imaging. Imaging is performed through a 2 mm craniotomy
553 in an anesthetized mouse. **b-c**, 2P imaging of a GFP-expressing interneuron 480 μm below the
554 brain surface (dura mater), before (b) and after F-SHARP (c). **d,** Cross-sectional plot along

555 the dotted lines in (b-c). F-SHARP images show a 5-fold increase of the signal in the
556 corrected region together with an enhancement of the resolution, demonstrated by the fact that
557 dendrites can be distinguished at the top of the cell after corrections (d). **e,** Correction pattern
558 applied on the SLM. **f-h,** Reconstructed E-field PSF at image plane (f) and real component of
559 the scattered (g) and corrected (h) 3D E-field PSF plotted along y-z plane. In (f), amplitude is
560 encoded in the brightness and phase in the colormap. Brightness has been saturated to 0.3 of
561 the maximum value to make the side lobes more clearly visible in (f) and to 0.5 of the
562 maximum value in (g) and (h). Scale bars, 20 µm in (b-c), 5 µm in (f-h).

563

564 **Figure 6 | Imaging through thinned mouse skull in vivo. a,** Schematic of imaging through
565 thinned skull (50 µm mean thickness) in an anaesthetized Thy1-YFP mouse. During imaging
566 we followed the same single apical dendrite 25 µm from the brain surface down to a depth of
567 325 µm. F-SHARP corrections were calculated every 50 µm and z-stack images were
568 acquired at ±25 µm around the correction plane. **b,** 3D rendering of the apical dendrite, before
569 (left) and after correction (right). **c-d,** 2P images before and after F-SHARP correction at
570 depths of z = 54 µm (top), z = 200 µm (middle) and z = 304 µm (bottom). The uncorrected 2P
571 images exhibit poor quality already at the superficial layers with the dendrite appearing as a
572 random speckle pattern. F-SHARP allows us to resolve the dendrite down to 325 µm and
573 single spines down to a depth of 200 µm, (d, middle). **e-f,** Correction pattern applied on SLM
574 (e) and reconstructed E-field PSF at corresponding depth. The reconstructed E-field PSF
575 appears as a random speckle pattern already at the more superficial layer, (f, top). The number
576 of corrected modes increases deeper into the brain (middle and bottom row). The streaking
577 artefacts in (f) are due to random tissue motion during recording and do not considerably
578 affect the reconstruction. Scale bars, 2 µm in (c-d), 5 µm in (f).

579

580 # Methods

581 ## Experimental setup

582 *F-SHARP modifications on an existing 2P microscope.* A conventional 2P microscope was
583 modified by introducing the following elements: a polarizing beamsplitter cube to split the
584 excitation beam (PBS252, Thorlabs, USA), a spatial light modulator (Pluto, Phase-only SLM,
585 Holoeye, Germany), a tip-tilt piezo-scanning mirror (S-334 Piezo Tip/Tilt Mirror, Physik
586 Instrumente, Germany), a phase-stepping piezo-scanner (S-314.10, Piezo Z-scanner, Physik
587 Instrumente, Germany), a recombining polarizing beamsplitter cube (PBS252, Thorlabs,
588 USA) and a polarizer (see Figure S1). The first polarizing beamsplitter splits the excitation
589 beam with one part (strong beam) directed towards the galvo scanning arm and the other
590 (weak beam) towards the piezo-scanning and phase stepper. The second polarizing
591 beamsplitter cube recombines the two beams before the scan lens and the polarizer is placed
592 at such angle in order to make the two beams interfere. During the measurement process the
593 strong beam is kept stationary in the FOV while the weak aberrated beam is scanned using the
594 piezo-scanners. The SLM was placed at the original galvo scanning arm and the strong beam
595 was corrected following each measurement. After the measurement of the E-field PSF is
596 finished, the final correction pattern is projected on the SLM with the strong beam forming a
597 sharp focus inside the scattering medium, the weak beam is blocked and the conventional
598 scanning arm (through the galvo mirrors) is used for 2P imaging. For a detailed description of
599 the experimental setup, see Supplementary Information.

600 *Imaging system in transmission.* The imaging system placed in transmission to better
601 characterize the F-SHARP system (Figure 3) is comprised of a 40x water immersion objective
602 (Nikon, CFI Apo 40x W NIR, NA=0.80) and a 200 mm tube lens (achromat doublet, f=200
603 mm, Thorlabs, USA) that project the image plane onto a CMOS camera sensor (Basler,
604 Germany).

605 ## Calculation of correction phase pattern

606 The measurement of the complex amplitude of the E-field PSF at the focal plane allows us to
607 compensate for scattering by using the process of Phase Conjugation. The complex-valued E-
608 field PSF is Fourier transformed (since the number of pixels measured is considerably smaller
609 than the pixels available on the SLM, we use zero padding before the Fourier transform). This
610 complex-valued correction pattern is resized to the appropriate size of the back aperture by
611 linear interpolation. The conjugate phase of the final resized correction field is then displayed
612 on the phase-only SLM.

613 **Alignment of F-SHARP**

614 F-SHARP directly measures the scattered E-field PSF inside the inhomogeneous medium
615 instead of scanning through the modes of the wavefront shaper. Therefore, in order to perform
616 optical phase conjugation and correct the scattered E-field PSF, the SLM has to be properly
617 aligned with respect to the back aperture of the objective. A known phase pattern was
618 projected onto the SLM and modulated the galvo-scanned beam (Supplementary Figure 2a).
619 We then set the galvo-scanned beam as the weak beam. We employed F-SHARP on a
620 uniform fluorescent sample and measured the E-field PSF of the modulated galvo scanned
621 beam (Supplementary Figure 2c). The Fourier transform of the E-field PSF is an image of the
622 back aperture of the objective lens (Supplementary Figure 2d). To finalize the alignment, we
623 mapped the measured back aperture to the SLM plane through an affine transformation and
624 corresponding z propagation. Alignment is considered satisfactory when the multiplication of
625 the complex conjugate of the reconstructed back aperture field with the complex pattern
626 projected onto the SLM yields a plane wave (Supplementary Figure 2b).

627 **Correction of system aberrations**

628 All conventional 2P images were acquired with the optical system aberrations corrected. The
629 system aberrations were estimated by, first projecting a flat phase onto the SLM and then
630 imaging a uniform fluorescent sample. Similar to the SLM alignment process we set the
631 galvo-scanned beam as the weak beam and used the other beam as the strong δ-like beam.
632 The Fourier transform of the reconstructed E-field PSF provided a map of the system
633 aberrations that was applied on all imaging and correcting experiments.

634 **Preparation of scattering samples**

635 *Fluorescent beads.* 1 μm red fluorescent beads (Latex beads, amine-modified polystyrene,
636 fluorescent red, Sigma-Aldrich, USA) were dried on top of a Type 1 coverslip. A droplet of
637 mounting medium (ProLong® Diamond Antifade Mountant, ThermoFisher Scientific, USA)
638 was placed on top and the sample was sealed with a Type 1 coverslip.

639 *Chicken muscle tissue.* Chicken breast tissue was cut perpendicular to the muscle fibers. The
640 sample was sandwiched between two Type 1 coverslips separated by a 0.5 mm silicon spacer.
641 The sample was then inspected under a light microscope to make sure it was free of air
642 bubbles.

643 *Fluorescein with sparse set of beads.* 1 μm red fluorescent beads (Latex beads, amine-
644 modified polystyrene, fluorescent red, Sigma-Alrdich, USA) were dissolved in a saturated
645 fluorescein solution (Sigma-Aldrich, USA) and dried on a Type 1 coverslip. A droplet of
646 mounting medium (ProLong® Diamond Antifade Mountant, ThermoFisher Scientific, USA)
647 was placed on top and the sample was sealed with a Type 1 coverslip.

648 *Scattering film.* A single layer of diffusing PARAFILM® M tape (measured thickness 125
649 µm) was placed on top of a Type 1 coverslip and was separated from the sample by 2 layers
650 of self-adhesive spacer (Secure-Seal™ Spacer, 9 mm diameter, 0.12 mm thickness,
651 Invitrogen, USA). The total separation distance between the scatterer and the sample was 0.58
652 mm (2 spacers, 2 x 0.12 mm and 2 coverslips, 2 x 0.17 mm). The volume between the spacers
653 was filled with water.

654 *Zebrafish larva imaging.* A 18 dpf zebrafish larva, expressing GCaMP6f under the NeuroD
655 promoter[45] was anesthetized by placing it in a 0.168 mg/ml solution of MS222 in fish water.
656 The anesthetized larva was then placed onto a petri dish with a droplet of 1% low melting
657 point Agarose (Sigma-Alrdich, USA) and mounted with the dorsal side towards the
658 microscope objective.

659 *Mouse surgery.* A 5 week old GAD67-GFP[47] and a 8 week old Thy1-YFP H[48] mouse were
660 used to test the performance of F-SHARP in mammalian brains in vivo. Mice were
661 anaesthetized with 1.5–2 % isoflurane. Mouse body temperature was monitored with a rectal
662 probe and maintained at 37°C using a heating pad. A lightweight metal head support was
663 implanted onto the skull with glue and dental cement. In the GAD67-GFP mouse, a 2 mm
664 diameter craniotomy was drilled over the primary somatosensory whisker barrel cortex (1.2
665 mm posterior, 3.5 mm lateral to Bregma) to expose the brain. Next, a 3 mm diameter glass
666 cover slip was placed on the brain surface. In the Thy1-YFP H mouse we carefully thinned
667 the skull above the primary somatosensory whisker barrel cortex to a thickness of about 50
668 µm. The skull was covered with Ringer's solution (in mM): 135 NaCl, 5 KCl, 5 HEPES, 1.8
669 $CaCl_2$, 1 $MgCl_2$.

670 All experimental procedures were carried out in accordance with the national and state
671 Animal Welfare Office.

672 **Parameters of imaging experiments**

673 The excitation wavelength for all reported experiments was 920 nm. The maximum power
674 used for all *in vivo* experiments was 25 mW. The intensity ratio between weak and strong
675 beam for all experiments was fixed to 1/30.

676

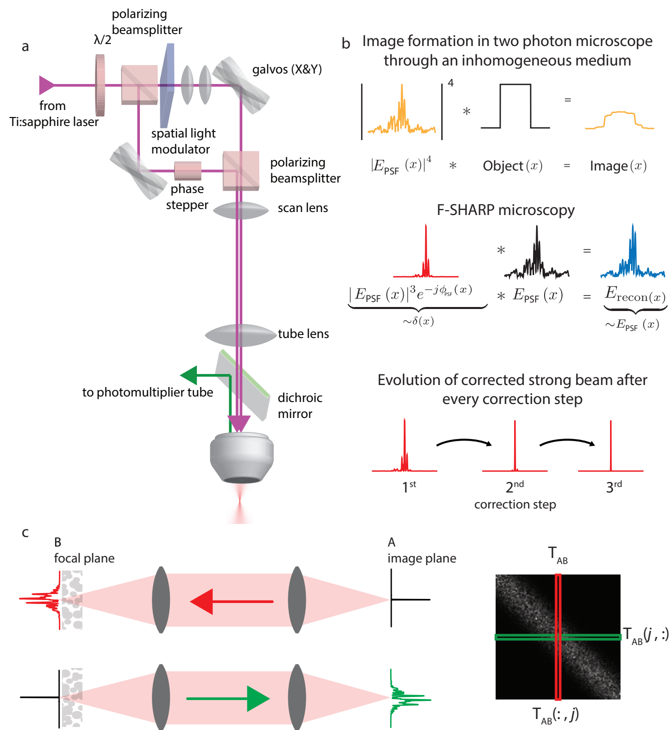

a
λ/2
polarizing beamsplitter
galvos (X&Y)
from Ti:sapphire laser
spatial light modulator
polarizing beamsplitter
phase stepper
scan lens
tube lens
to photomultiplier tube
dichroic mirror
b
Image formation in two photon microscope through an inhomogeneous medium
$|E_{PSF}(x)|^4$ * Object(x) = Image(x)
F-SHARP microscopy
$\underbrace{|E_{PSF}(x)|^3 e^{-j\phi_{PSF}(x)}}_{\sim\delta(x)} * E_{PSF}(x) = \underbrace{E_{recon}(x)}_{\sim E_{PSF}(x)}$
Evolution of corrected strong beam after every correction step
1st
2nd correction step
3rd
c
B focal plane
A image plane
T_{AB}
$T_{AB}(j,:)$
$T_{AB}(:,j)$

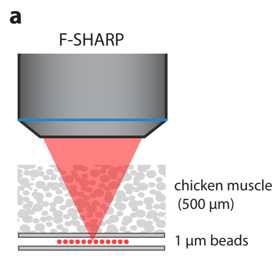
a
F-SHARP
chicken muscle
(500 µm)
1 µm beads

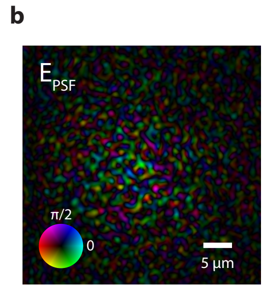
b
E PSF
π/2
0
5 µm

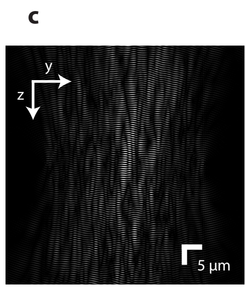
c
y
z
5 µm

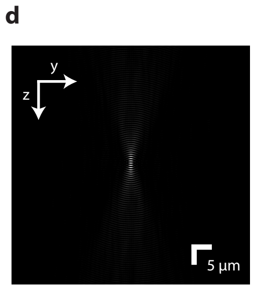
d
y
z
5 µm

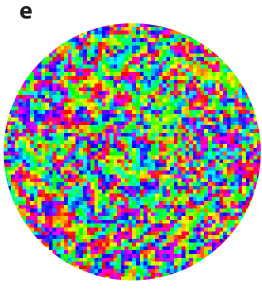
e

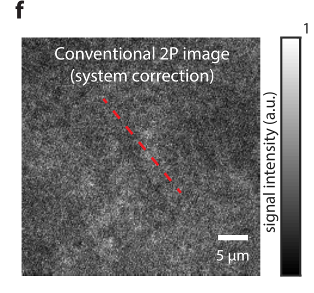
f
Conventional 2P image
(system correction)
5 µm
signal intensity (a.u.)
1

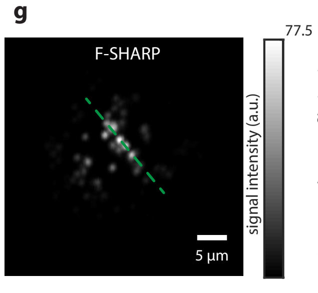
g
F-SHARP
5 µm
signal intensity (a.u.)
77.5

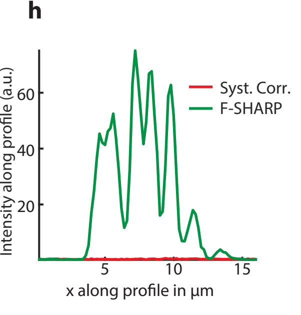
h
Syst. Corr.
F-SHARP
Intensity along profile (a.u.)
20
40
60
5
10
15
x along profile in µm

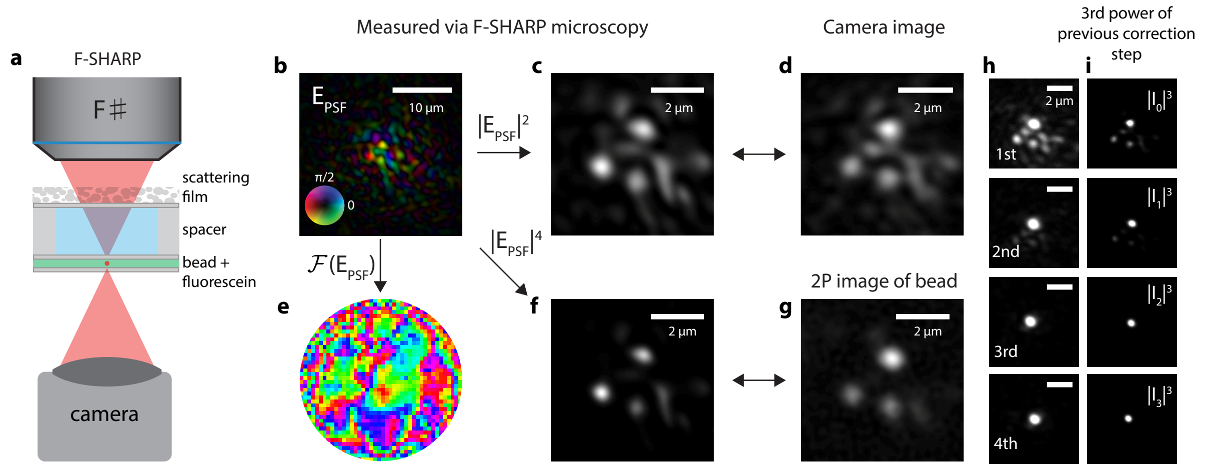
a
F-SHARP
F♯
scattering film
spacer
bead + fluorescein
camera
Measured via F-SHARP microscopy
b
E_PSF
10 µm
π/2
0
|E_PSF|^2
|E_PSF|^4
F(E_PSF)
e
c
2 µm
f
2 µm
Camera image
d
2 µm
2P image of bead
g
2 µm
3rd power of previous correction step
h
2 µm
1st
2nd
3rd
4th
i
|I_0|^3
|I_1|^3
|I_2|^3
|I_3|^3

a
F-SHARP
agarose
18 dpf zebrafish larva
b
10 µm
Conventional 2P image
(system correction)
intensity (a.u.)
1
0
c
10 µm
F-SHARP
1
0
d
E_{PSF}
5 µm
π/2
0
e
10 µm
Conventional 2P image
(system correction)
0.5
0
f
10 µm
F-SHARP
0.5
0
g
h
y
z
5 µm
i
y
z
5 µm

a
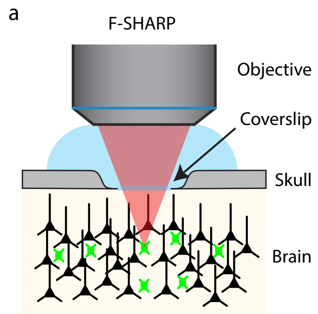

b
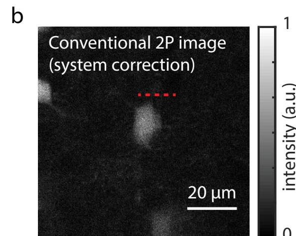

c
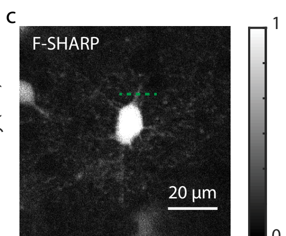

d
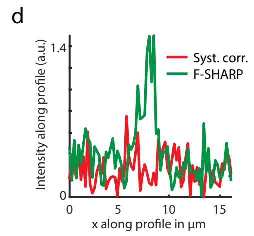

e
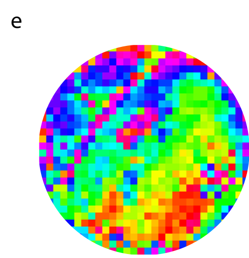

f
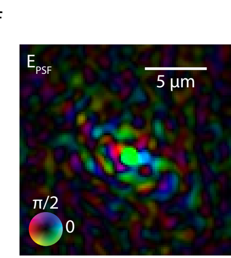

g
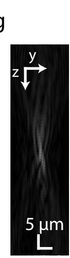

h
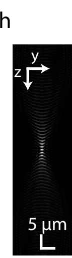

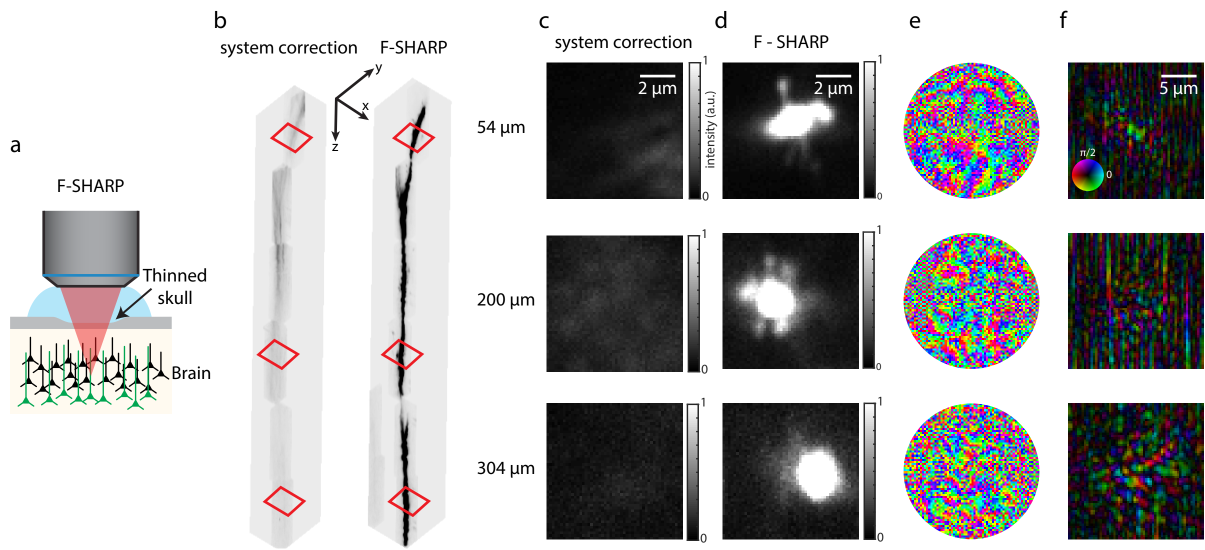
a
F-SHARP
Thinned skull
Brain
b
system correction
F-SHARP
y
x
z
c
system correction
d
F - SHARP
e
f
2 µm
5 µm
intensity (a.u.)
54 µm
200 µm
304 µm
π/2
0
1